www.sciencemag.org/cgi/content/full/science.1252418/DC1

Supplementary Materials for

Oceanic Mass Transport by Mesoscale Eddies

Zhengguang Zhang, Wei Wang,* Bo Qiu

*Corresponding author. E-mail: wei@ouc.edu.cn

Published 26 June 2014 on *Science* Express
DOI: 10.1126/science.1252418

This PDF file includes:

Materials and Methods

Data

Five datasets are utilized in this study: satellite altimetry sea surface height data, Argo profiling float temperature and salinity (T/S) data, WOA05 climatological T/S data, Arabian Sea Experiment mooring data, and Kuroshio Extension System Study (KESS) mooring data. All these datasets are publicly downloadable from Internet.

For the altimetry SSH data, we use the delayed-time product produced by AVISO (available at: http://www.aviso.oceanobs.com). The AVISO dataset consists of the globally gridded sea level anomaly (SLA) field from multiple simultaneously operating satellites, with a 0.25° ×0.25° spatial resolution. The time-span is from Oct 1992 to Jan 2010, with a 7-day temporal resolution. The SLA field is defined to be the residuals relative to the 7-year (i.e., 1993-1999) mean.

The Argo profiling float data is provided by China Argo Real-time Data Center (http://www.argo.gov.cn/argo-eng/index.asp). The dataset consists of about 600,000 T/S profiles in the upper 2,000 m between 1996 and 2010, with time and location of each profile recorded. These T/S data have been subject to real-time quality control (*SI*). From the T/S profiles, the potential density ρ profile relative to the sea surface (density for short hereafter) can be readily calculated.

The World Ocean Atlas 2005 data is provided by National Oceanographic Data Center (http://www.nodc.noaa.gov/OC5/WOA05/pr_woa05.html), and the objectively analyzed 1° gridded climatological T/S field is used here. We mainly use the seasonal mean field, and also compute the potential density from temperature and salinity field relative to the sea surface.

The Arabian Sea Experiment mooring data is provided by Woods Hole Oceanographic Institution (http://uop.whoi.edu/archives/arabiansea/arabiansea.html). The mooring was located at 30.5°N, 61.5°E and collected vertical T/S profiles during October 1994 to October 1995.

The Kuroshio Extension System Study (KESS) project provides 2 years of subsurface mooring data (available at: http://uskess.org/data_public.html). The mooring system was deployed in the Kuroshio Extension region near 34°N 146°E during May 2004 to May 2006.

Reconstruct Eddy Density Field

Reconstruction of the eddy density field is divided into three steps: First, identify eddies from the weekly altimetry SLA maps, and determine the SLA value at the eddy's center and their radius. Then, use the available Argo density profiles to composite the normalized, three-dimensional (3-D) structure of the eddy's density anomaly field. Finally, combine the altimetry SLA signal and the composite eddy density structure to reconstruct the density field for individual eddies.

In order to identify the eddies from altimetry, we search localized extremes of SLA first. If an extreme point is surrounded by closed contours of Okubo-Weiss parameter $W = -2 \times 10^{-12}\ s^{-1}$ (*S2, S3*), this point is then recognized as an eddy center. The Okubo-Weiss parameter is given by (*S4, S5*):

$$W = 4(u_x^2 + v_x u_y) \tag{1}$$

where the horizontal velocities are calculated by geostrophic balance $u = -(g/f)\eta_y$ *and* $v = (g/f)\eta_x$,(η is SLA, g is gravity acceleration), and the subscripts x and y represent the zonal and meridional spatial derivatives, respectively. The radius of the eddy R_0 is given by the equal-area circle of the closed W contour surrounding the eddy center (*S6*), and the SLA at the eddy's center η_0 is directly evaluated from the altimetry maps.

To derive the vertical structures of the mesoscale eddies, we follow the composite analysis approach of (*S7*) based on the Argo profiling float data. Specifically, after constructing its density structures from the T/S profiles, the eddy's density anomaly profile $\rho_e(z)$ is calculated relative to the local seasonal mean density profile from the WOA climatology. The Argo float-derived density anomaly profile is then projected onto the eddy-center coordinate, with the distance to the eddy center r as the horizontal ordinate and depth z as the vertical ordinate. Considering the eddy structure variations in different regions, the composition is conducted in a 30°latitude×30°longitude box. This size of the region is big enough to ensure there are enough Argo profiles to perform the composition, but small enough to avoid smearing out of eddy structures. The composite density anomaly profile in a region is constructed by double normalization, with the horizontal scale normalized by the eddy radius R_0 and the amplitude normalized by SLA at the eddy center η_0:

$$\rho_n(r_n, z) = \eta_0^{-1} \cdot \rho_e(r / R_0, z) \tag{2}$$

where $r = (x^2 + y^2)^{1/2}$ is the distance to the eddy center, $r_n = r/R_0$ is the normalized distance, and (x,y) are the zonal and meridional ordinates relative to the eddy center. Our former study (*S7*) indicates that the variables (r_n,z) for the normalized density anomaly field are functionally separable:

$$\rho_n(r_n; z) = R(r_n) \cdot H(z) \tag{3}$$

where $R(r_n)$ provides the radial structure and $H(z)$ the vertical structure. According to our former study (*S7*), the radial structure of eddy can be described by a universal analytic function: $R(r_n) = (1-r_n^2/2)\exp(1-r_n^2/2)$, and this function is used in our reconstruction procedures. The vertical structures of mesoscale eddies obtained in the regional composite analysis are recorded in a 1° x 1° global grid.

With the regional composite eddy structure and the radius R_0 and center SLA η_0 of an eddy identified by altimetry, the density anomaly field of the individual eddy can be reconstructed by $R(r_n)$ and $H(z)$ *specific* to the nearest grid point:

$$\rho_e(r, z) = \rho_e(r_n \cdot R_0, z) = \eta_0 \cdot R(r_n) \cdot H(z) = \eta(r) \cdot H(z) \tag{4}$$

where $\eta(r)$ is the radial structure of SLA. By adding the background seasonal density profile $\bar{\rho}(x,y,z)$ to $\rho_e(r, z)$, the total density field $\rho(x,y,z)$ of the eddy is obtained. *All* mesoscale eddies have a universal structure in normalized stretching coordinate (*S7*), however, the reconstructed density structure $\rho(x,y,z)$ is different for each individual eddies.

Validation of the Reconstruction Method

Since the accuracy of the potential vorticity field is highly dependent on the reconstructed density field, we use *in situ* mooring observations from three sites to validate our reconstruction method.

The first mooring system is deployed at 60.6°N, 52.4°W in the Labrador Sea from September 2007 to September 2009 (*S8*). This 2-year mooring measurements captured 12 warm-core eddies, and the detailed information of SLA at the eddy center, the radius of eddy and the countercurrent isopycnal displacement is available in (*S8*). We first take a warm-core eddy captured by the mooring at October 11 2008 as an example, with a center SLA $\eta_0 = 0.081\ m$ and eddy radius $R_0 = 20\ km$. First, use the universal radial structure of eddy to reconstruct its SLA distribution:

$$\eta(r) = \eta_0 \cdot \left[1 - \frac{1}{2}\left(\frac{r}{R_0}\right)^2\right] \cdot \exp\left[1 - \frac{1}{2}\left(\frac{r}{R_0}\right)^2\right] \quad (5)$$

Then, get the regional composite vertical structure of eddy $H(z)$ at the grid point 61°N, 52°W. The density structure of this eddy can be calculated by $\rho_e(r, z) = \eta(r)\, H(z)$. Finally, combining the winter background density profile $\bar{\rho}(x,y,z)$from WOA data, the eddy density field is reconstructed by: $\rho(r,z) = \rho_e(r,z) + \bar{\rho}(x,y,z)$, as shown in Fig.1A in the main text. Notice that with the mooring provides only the time series of density profiles, the time has been transformed into distance by the horizontal propagation speed (25.8 cm s^{-1}) of the eddy. The density structures of the other 11 warm-core eddies are reconstructed in the same way. Figure 1C in the main text compares the observed and reconstructed 27.7 kg m^{-3} isopycnal displacement at the eddy center as blue points.

The second mooring located at 15.5°N 61.5°E is from the Arabian Sea Experiment. During its one-year deployment, two cold-core eddies and one warm-core eddy were observed. The first cold-core eddy is observed on November 30 1994, and its density field is reconstructed and compared with the *in situ* density section from the mooring as an example of cold-core eddy in Fig.1B. The observed 26.0 kg m^{-3} isopycnal displacement at the eddy center is 73.7 m and the corresponding reconstructed displacement is 65.7 m. The other cold-core eddy and the warm-core eddy were observed on August 30, and July 5, 1995, respectively. The observed and reconstructed 26.0 kg m^{-3} isopycnal displacements of these three eddies are compared in Fig.1C as black squares.

The third mooring is from the KESS project, which used a subsurface profiler on the moorings to observe temperature and salinity. There are a total of eight moorings (K1-

K8), but it seems that the profilers did not work well during strong eddy events. After checking the records of the eight moorings, only two warm-core eddy observations can be used to validate our reconstruction method. The first warm-core eddy was observed by the K3 mooring at 146.9E 35.5N on March 15, 2006 and the second warm-core eddy by the K4 mooring at 146.2E 35.2N on February 9, 2005. The reconstructed 27.4 kg m^{-3} isopycnal displacements of these two eddies are compared with their observed values in Fig.1C with red triangles.

The comparisons shown in Fig.1C indicate that the relative error of the reconstructed density field is about 20% of the observed variance. It is important to mention that our verification covers the low-, mid- and high-latitude regions in the Pacific, Atlantic and Indian Oceans. It also involves both polarities of the mesoscale eddies (unfortunately only two cold-cold eddies out of the 17 eddy samples are available for validation). We believe the 20% relative error is sufficiently small that validates the reconstruction method adopted in this study.

The Potential Vorticity Field

We estimate the potential vorticity (PV) q by following its definition:

$$q = \frac{(f+\omega)\rho_z}{\rho_0} \tag{6}$$

where ω is relative vorticity, ρ_z is vertical gradient of density, ρ_0 is mean density and f is the Coriolis parameter. Following a fluid particle, q is conserved if the environment is inviscid and adiabatic.

With ρ_z calculated from the reconstructed eddy density field, the only unknown quantity in (6) is relative vorticity. To estimate the relative vorticity, we use the reconstructed eddy density anomaly field $\rho_e(r,z) = \eta(r)\, H(z)$ to first compute the eddy pressure anomaly field $p_e(r,z) = \eta(r)\, P(z)$ through hydrostatic balance with a reference level at 2,000 m, where $P(z)$ is:

$$P(z) = -\int_{-2000}^{z} g \cdot H(z')dz' \tag{7}$$

and g is the gravity acceleration. Then we use the geostrophic balance to compute the horizontal velocity from the eddy pressure anomaly field relative to 2000m. Finally, we take the curl of the geostrophic velocity field and obtain the relative vorticity $\omega(r,z) = L(r)\, P(z)$, where $L(r)$ is the radial structure of relative vorticity :

$$L(r) = \frac{1}{f\rho}\frac{1}{r}\frac{\partial}{\partial r}\left(r\frac{\partial \eta}{\partial r}\right) \tag{8}$$

Notice that calculating the radial structure of relative vorticity here does not involve detailed SSH information, we only need the altimeter data for the SLA at the eddy center η_0 and the radius of the eddy R_0, and the universal radial structure of the mesoscale eddies has been found rather stable (*S7, S9*). The main error source for the relative vorticity is the assumption of level of no-motion at 2000 m. Many eddies in the ACC region have

considerable barotropic, non-zero, horizontal velocity at 2000 m. Based the information of Argo float trajectories at their 2000 dbar parking depth, we estimate our calculation of relative vorticity has a relative error at the 15%-20% level.

With both ρ_z and relative vorticity evaluated, the three-dimensional PV field can be computed. After projecting the PV distribution onto the isopycnal surfaces, we determine the fluid trapped by the mesoscale eddies by searching for closed PV contours. Due to the relative vorticity and squeezing/stretching of the water column, the PV contours near the core of an eddy can enclose upon themselves, forming closed PV contours. In contrast, the β effect and the large-scale isopycnal slopes of the background PV field works to suppress the formation of closed PV contours. It is the competition of the eddy perturbation PV field versus the large-scale background PV field that determines the area of the fluid trapped by closed PV contours on each isopycnal surface. Figure 2A (2B) in the main text shows the three-dimensional shape of the fluid trapped by a warm-core (cold-core) eddy and the PV distributions on representative isopycnals. Since PV is a dynamical quantity, its close contours and corresponding trapped volume are independent of the eddy propagation speed and the choice of reference frame.

Two approximations involved in our estimation of eddy volume need to be clarified. The first is the radial symmetric approximation. The main task of this study is to estimate the eddy-induced transport in a statistical sense, and the radial symmetric approximation has been statistically validated by a former study of altimetry data (S9). The second is we do not consider tilting of the eddy vertical structure. Tilting of the eddy vertical structure is important when considering the tracer transport by mesoscale eddies with a horizontal background tracer gradient. The fluid volume trapped by eddies is determined by areas surrounded by the outermost close PV contours on each isopycnal surfaces; as such, the tilting of eddy vertical structure has little impact on the estimation of eddy-induced volume transports.

Eddy Propagation Speed

Propagation speed of individual eddies can be calculated by tracking their trajectories in sequential altimetry SLA maps (*S6, S9*). In order to obtain the global distribution of the eddy propagation speed, we set up a globally uniform 2° × 2° grid. For each gird, we calculate the eddy propagation speed by averaging the propagation speeds of all eddies within a 4° ×4° average-bin.

Figure S1A shows the global distribution of the zonal eddy propagation speed C_x .In Fig.S1B, we compare the average zonal propagation speed from our calculation and that from (*S9*). The two estimates are largely consistent. In most parts of the world oceans, eddies move westward and tend to have a larger speed in lower latitudes. The exception is along the Antarctic Circumpolar Current (ACC) where strong background time-mean current advects eddies eastward.

The meridional propagation speed of mesoscale eddies C_y is also calculated and its global distribution is shown in Fig.S2A, and its zonal average is shown in Fig.S2B. Meridionally, mesoscale eddies have a tendency to move poleward within the tropics (20°S-20°N), and equator-ward in the subtropical regions. This tendency is consistent with the average equatorward deflection of all the eddies with lifetimes of 16 weeks and longer in the subtropical regions obtained by (*S9*). While an interesting result, the meridional propagation speed of the mesoscale eddies is one order of magnitude smaller than the zonal propagation speed and, as a result, it plays a less important role in volume transport.

Global Distribution of Volume Trapped by Mesoscale Eddies

For each weekly SLA map, we calculate the volume trapped by each eddy by using the reconstruction method and PV criterion. The altimetry data used in this study contains *N=908* snapshots from Oct 1992 to Jan 2010. For each snapshot and each selected average-bin of 1000 km x 1000 km, the total volume V (unit: m^3) trapped by mesoscale eddies is first calculated. Accumulating the total trapped volume by eddies within the bin for the whole time range from Oct 1992 to Jan 2010, and dividing it by the number of snapshots give the time averaged eddy-trapped volume:

$$V_{ave} = \sum V / N \tag{9}$$

Repeating this process for every grid point lead to the global distribution of V_{ave} (unit: m^3) shown in Fig.S3.

Denser eddy population and more fluid trapped by individual eddies lead to a larger average eddy-trapped volume. In the north hemisphere, the average eddy-trapped volume tends to be large on the west side of the ocean basins. Hot spots appear near the west boundary currents, such as the Kuroshio Extension and the Gulf Stream. However, the average eddy-trapped volume tends to be smaller within the cores of the strong background currents when compared with their nearby regions. This is caused by steep sloping of the background isopycnal surfaces along the cores of the western boundary currents. The steep isopycnal sloping leads to a large background PV gradient, suppressing the ability of eddies to trap fluid. In the ACC region, hot spots of the average eddy-trapped volume are all located near the large topographic features. This is likely due to the perturbation of background PV gradient and the enhanced eddy generation near these large topographies.

Eddy-induced Volume Transport

After estimation of the trapped volume V and the zonal propagation speed C_x of individual eddies, we calculate the global distribution of the eddy-induced zonal transport by the following steps. First, we lay out a uniform 2° ×2° global grid, then set up an average-bin with a 10° meridional width and a 20° zonal length around each grid point, and record its zonal length as D_{lon} (unit: m, the length of 20° longitude at each grid point).

For every eddy identified in the weekly altimetry maps, the volume transport carried by this eddy is V^*C_x. Accumulating the total transport by the eddies within this bin for the whole time period from Oct 1992 to Jan 2010, then dividing it by the number of the SLA snapshots, the zonal length D_{lon} and meridional width 10°, give the average eddy-induced zonal transport across the 1°-latitude section:

$$Q_x = \frac{\sum V \cdot C_x}{10^o \cdot N \cdot D_{lon}} \tag{10}$$

Figure 3A in the main text shows the global distribution of Q_x in unit of Sv per degree (1 Sv = 10^6 m^3 s^{-1}).

If we further divide the transport into the eastward component (Q_x>0) and westward component (Q_x<0), and integrate them over the whole latitude range:

$$Q_w(\phi) = \int_{Q<0} Q_x(\phi,\theta)\cdot d\theta \qquad Q_e(\phi) = \int_{Q>0} Q_x(\phi,\theta)\cdot d\theta \tag{11}$$

give the integral eastward transport Q_e and westward transport Q_w, respectively. In equation (11), (ϕ,θ) are longitude and latitude, respectively. We can also compute the meridional integrated transport north and south of 40ºS:

$$Q_n(\phi) = \int_{-40}^{80} Q_x(\phi,\theta)\cdot d\theta \qquad Q_s(\phi) = \int_{-80}^{40} Q_x(\phi,\theta)\cdot d\theta \tag{12}$$

and we compare Q_w/Q_e and Q_n/Q_s in Fig.3B.

Similar to Q_x, we can also compute the eddy-induced meridional transport Q_y (across the 1°-longitude section) within the same average-bin:

$$Q_y = \frac{\sum V \cdot C_y}{20^o \cdot N \cdot D_{lat}} \tag{13}$$

where D_{lat} (unit: m) is the meridional length of the bin. The global distribution of Q_y is shown in Fig.4A. For the meridional transport, we can calculate its zonal integrated transport:

$$Q_Y(\theta) = \int_{0}^{360} Q_y(\phi,\theta)\cdot d\phi \tag{14}$$

The zonal integrated eddy-induced meridional transport is shown in Fig.4B. Due to the small meridional propagation speed of eddies; the eddy-induced meridional transport is much smaller than the zonal eddy-induced transport.

The main focus of this paper is to estimate the global eddy-induced volume transport in the sense of statistical mean. To quantify the estimation errors on such a global scale is rather difficult. On the other hand, there are independent estimations of eddy-induced volume transport based on *in situ* observations available in some specific regions and this provides us with a chance to indirectly evaluate the error bounds in our estimations. Castelao (*S10*) estimated the eddy-induced onshore transport in the South Atlantic Bight and Gulf Stream Recirculation region (28°N-35°N, west of 75.5°W) to be 7.6 ± 2.2 Sv by

combining the altimeter and Argo float data, and our estimated eddy induced transport at the same location is 6.1 Sv. There are also several observations available in the Agulhas Current regions. By combining hydrographic profiles and lower-ADCP data, Gazoli et al. (*S10*) estimated the eddy induced inter-ocean transport from the Indian Ocean into the Atlantic Ocean is about 6-10 Sv. Richardson (*S11*) used the subsurface float and surface drifter data and estimated the eddy induced inter-ocean transport to be about 10-13 Sv. With the altimeter data and assumed eddy vertical structures, Dencausse et al. (S12) estimated the eddy induced Agulhas inter-ocean transport to be about 8.5 Sv. Finally, a recent estimation based on altimeter and Argo floats by Souza et al. (S13) finds the inter-ocean transport at 9 ± 8 Sv. Our estimation of the eddy induced inter-ocean transport is 8.2 Sv. From these comparisons, we expect our global estimation of eddy-induced transport to have a relative error about 20%.

Finally, there is an assumption in our calculation of SLA at the eddy's center η_0, which ignores the variation of the large-scale SSH field (the seasonal steric signal, for example, is contained in the SLA maps we used). In order to evaluate the influence of this assumption to the eddy-induced transport, we introduce η_a, the difference between the SLA at the eddy's center and the mean SLA around the eddy edges (at $3.5*R_0$ where the eddy perturbations largely vanish) as another metric for eddy amplitude. We choose a snapshot of SLA and identify all eddies in it, then we compare η_0 and η_a of these eddies in Fig.S4A, which indicates the potential relative error in eddy amplitude is about 20%, and this may cause bias and overestimate of the volume trapped by individual eddies. Then we use η_0 and η_a to estimate the volume trapped by these eddies respectively and compare them in Fig.S4B, which indicates the bias in estimating the volume trapped by *individual eddies* is about 25% of its variation. Chelton et al. (*S9*) found that the large-scale SSH variations may be the main cause for this bias. For example, if the large-scale SSHA is positive in a selected region at a given time, it will lead to overestimation of the volume trapped by cold-core eddies and underestimation of the volume trapped by warm-core eddies in the same region. And the negative large-scale SSHA has an opposite effect. Considering there will be both warm/cold core eddies in a region, the bias of volume trapped by warm/cold core eddies will compensate each other when we perform the large-sample statistical average. Thus, we expect the error caused by the variation of large-scale SSH field to the global estimation of eddy-induced transport to be small.

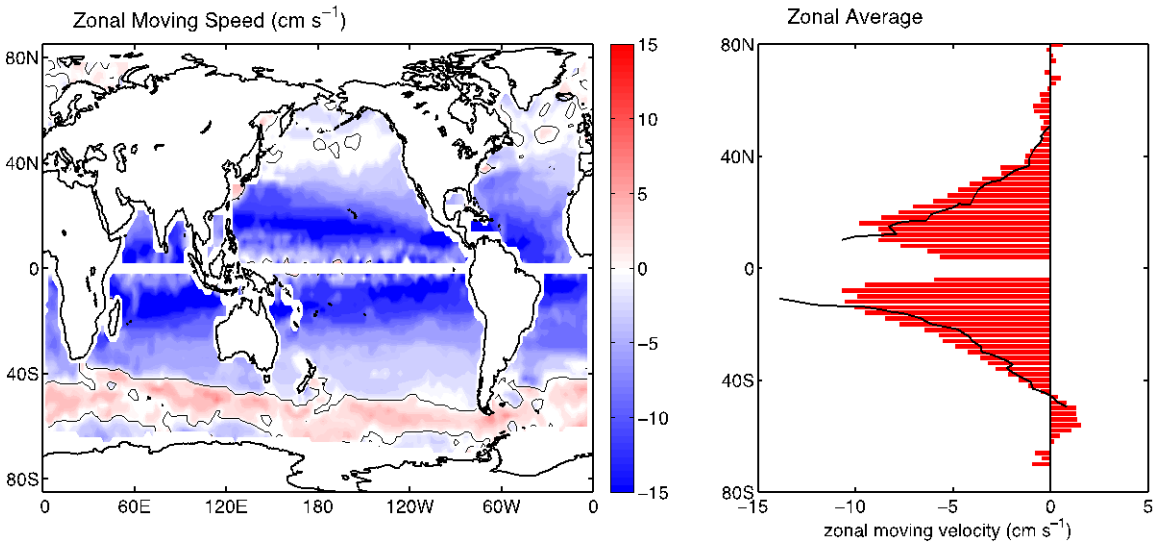

Fig. S1.

(A) Global distribution of the zonal propagation speed of mesoscale eddies. The zonal propagation speed is obtained by tracking eddies from satellite altimetry data of 1992 - 2010. Thin lines represent the zero zonal speed contours. **(B)** The zonal average of zonal propagation speed of mesoscale eddies. The red bars represent the latitude distribution of our results, and the solid black curve represents the results from (*S9*).

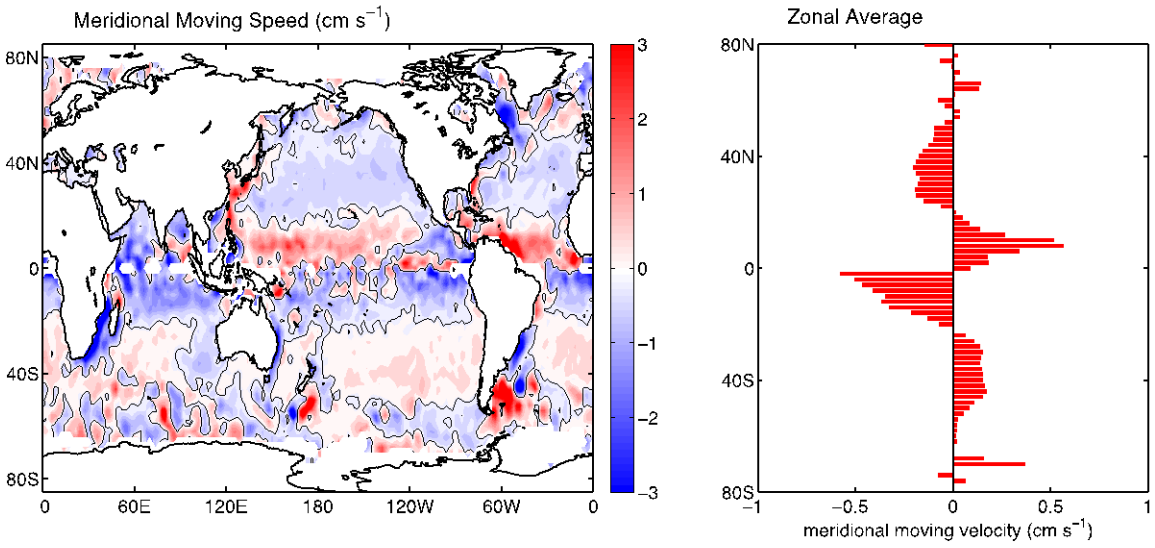

Fig. S2.

(A) Global distribution of the meridional propagation speed of mesoscale eddies. The meridional propagation speed is obtained by tracking eddies from satellite altimetry data of 1992 - 2010. Thin curves represent the zero zonal speed contours. **(B)** The zonal average of meridional propagation speed of mesoscale eddies.

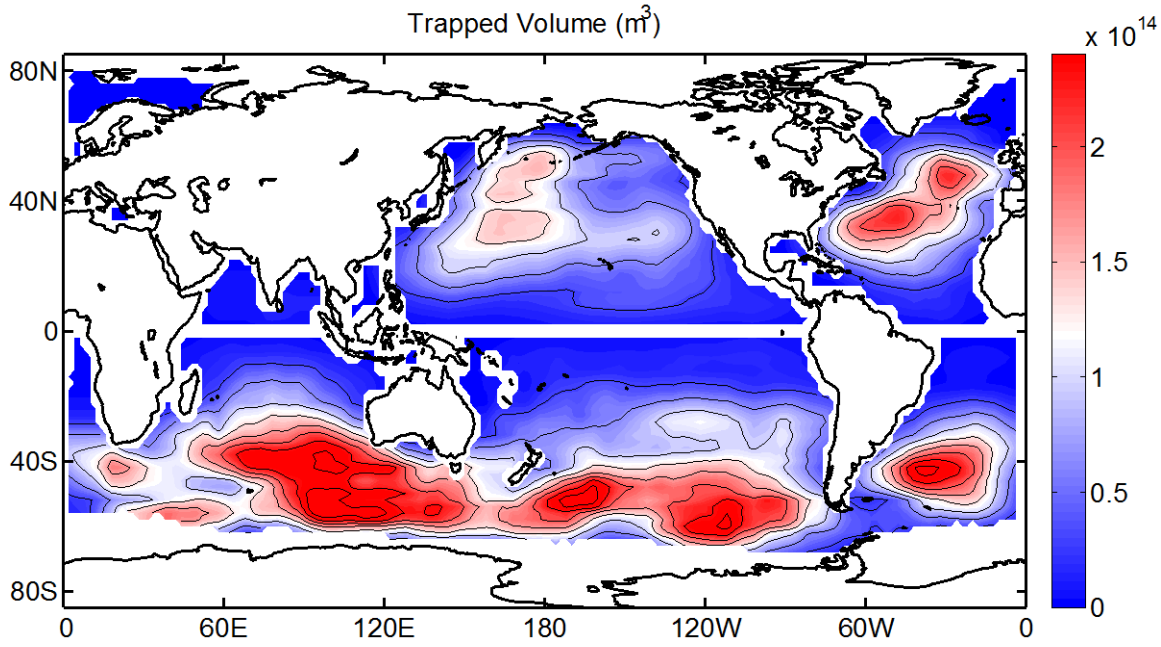

Fig. S3.

Global distribution of volume of the fluid trapped by mesoscale eddies. The volume is obtained by averaging the total volume simultanously trapped by mesoscale eddies within 1000km×1000km rectangle region around each grid point. Contour interval is 3×10^{13} m^3.

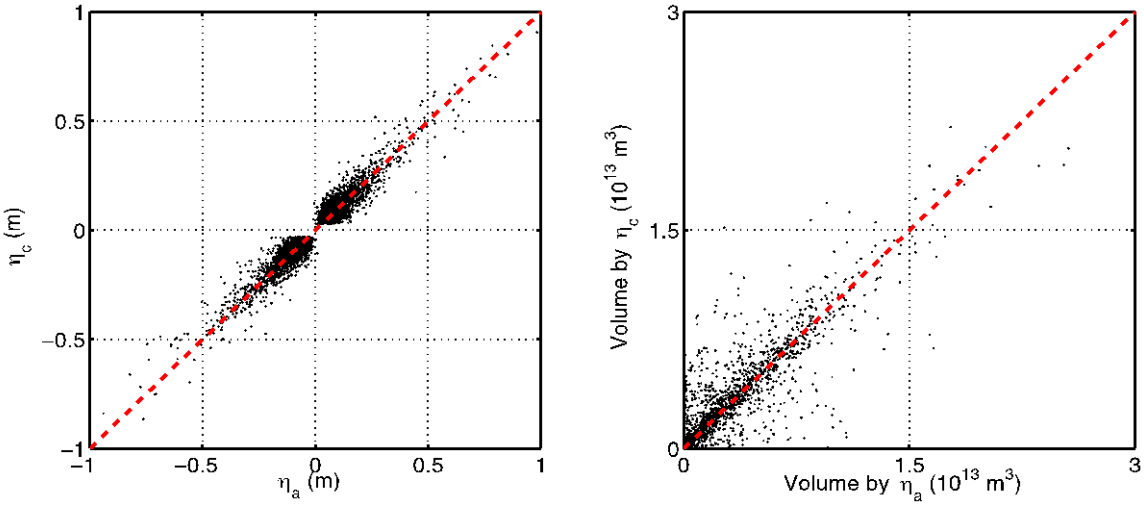

345

346 **Fig. S4.**

347 **(A)** The comparison between SLA at eddy-center η_0 and the SLA difference η_a betweem
348 the eddy center and on the eddy edges. **(B)** The comparison of trapped volumes by
349 individual eddies calculated from η_0 and η_a, respectively.

350

References

S1. G. H. Wang et al., *User's Manual of a Global Argo Profiling Observations Dataset Based on New Quality Control*. (available online: ftp://ftp.argo.org.cn/pub/ARGO/G-argo/Argo-dataset/Argo-dataset.pdf), pp. 15.

S2. A. Chaigneau, G. Eldin, B. Dewitte, Eddy activity in the four major upwelling systems from satellite altimetry (1992–2007), *Prog. Oceanogr*. **83,** 117–123 (2009).

S3. A. Chaigneau et al., Vertical structure of mesoscale eddies in the eastern South Pacific Ocean: A composite analysis from altimetry and Argo profiling floats, *J. Geophys. Res*. **116**, C11025, doi:10.1029/2011JC007134 (2011).

S4. J. Isern-Fontanet, E. Garcia-Ladona, J. Font, Identification of marine eddies from altimetric maps, *J. Atmos. Oceanic Technol*. **20**, 772– 778 (2003).

S5. J. Isern-Fontanet, E. Garcia-Ladona, J. Font, Vortices of the Mediterranean Sea: An altimetric perspective, *J. Phys. Oceanogr.* **36**, 87– 103 (2006).

S6. D. B. Chelton, M. G. Schlax, R. M. Samelson, R. A. de Szoeke, Global observations of large oceanic eddies. *Geophys. Res. Lett*. **34**, L15606, doi:10.1029/2007GL030812. (2007).

S7. Z. G. Zhang, Y. Zhang, W. Wang, R. X. Huang, Universal structure of mesoscale eddies in the ocean. *Geophys. Res. Lett*. **40**, 3677-3681 (2013).

S8. M. F. de Jong , A. S. Bower, H. H. Furey, Two years of observations of warm-core anticyclones in the Labrador Sea and their seasonal cycle in heat and salt stratification. *J. Phys. Oceanogr*. **44,** 427-443 (2014).

S9. D. B. Chelton, M. G. Schlax, R. M. Samelson, Global observations of nonlinear mesoscale eddies. *Prog. Oceanogr*. **91**,167-216 (2011).

S10. R. M. Castelao, Mesoscale eddies in the South Atlantic Bight and the Gulf Stream Recirculation region: Vertical structure. *J. Geophys. Res. Oceans*, **119**, 2048-2065 (2014).

S10. S. L. Garzoli et al., Three Agulhas rings observed during the Benuela Current Experiment. *J. Geophys. Res.* **104**, 20971-20985 (1999).

S11. P. L. Richardson, Agulhas leadkage into the Atlantic estimated with subsurface floats and surface drifters, *Deep Sea Res., Part I,* **54**, 1361-1389 (2007).

S12. G. Dencausse, M. Arhan, S. Speich, Routes of Agulhas rings in the southeastern Cape Basin, *Deep Sea Res., Part I,* **57**, 1406-1421 (2010).

S13. J. M. A. C. Souza, C. de Boyer Montegut, C. Cabanes, P. Klein, Estimation of the Agulhas ring impacts on meridional heat flux and transport using ARGO floats and satellite data. *Geophys. Res. Lett*. **38**, L21602, doi:10.1029/2011GL049359 (2011).